Journal of Power Sources 196 (2011) 10328–10335

Contents lists available at SciVerse ScienceDirect

Journal of Power Sources

journal homepage: www.elsevier.com/locate/jpowsour

Evaluation of commercial lithium-ion cells based on composite positive electrode for plug-in hybrid electric vehicle applications. Part I: Initial characterizations

Matthieu Dubarry[a], Cyril Truchot[a], Mikaël Cugnet[a], Bor Yann Liaw[a,*], Kevin Gering[b], Sergiy Sazhin[b], David Jamison[b], Christopher Michelbacher[b]

[a] Hawaii Natural Energy Institute, SOEST, University of Hawaii at Manoa 1680 East-West Road, POST 109, Honolulu, HI 96822, USA
[b] Energy Storage & Transportation Systems, Idaho National Laboratory, P.O. Box 1625, Idaho Falls, ID 83415-2209, USA

ARTICLE INFO

Article history:
Received 20 June 2011
Received in revised form 18 August 2011
Accepted 18 August 2011
Available online 25 August 2011

Keywords:
Lithium-ion battery
Composite electrode
PHEV
Cell-to-cell variations
Incremental capacity

ABSTRACT

Evaluating commercial Li-ion batteries presents some unique benefits. One of them is to use cells made from established fabrication process and form factor, such as those offered by the 18650 cylindrical configuration, to provide a common platform to investigate and understand performance deficiency and aging mechanism of target chemistry. Such an approach shall afford us to derive relevant information without influence from processing or form factor variability that may skew our understanding on cell-level issues. A series of 1.9 Ah 18650 lithium ion cells developed by a commercial source using a composite positive electrode comprising $\{LiMn_{1/3}Ni_{1/3}Co_{1/3}O_2 + LiMn_2O_4\}$ is being used as a platform for the investigation of certain key issues, particularly path-dependent aging and degradation in future plug-in hybrid electric vehicle (PHEV) applications, under the US Department of Energy's Applied Battery Research (ABR) program. Here we report in Part I the initial characterizations of the cell performance and Part II some aspects of cell degradation in 2C cycle aging. The initial characterizations, including cell-to-cell variability, are essential for life cycle performance characterization in the second part of the report when cell-aging phenomena are discussed. Due to the composite nature of the positive electrode, the features (or signature) derived from the incremental capacity (IC) of the cell appear rather complex. In this work, the method to index the observed IC peaks is discussed. Being able to index the IC signature in details is critical for analyzing and identifying degradation mechanism later in the cycle aging study.

1. Introduction

Rechargeable lithium-ion batteries (LIB) are viable choices for numerous energy storage and mobile power applications. Most notably in the transportation sectors, plug-in hybrid electric vehicles (PHEVs) are of great interest in using LIB for propulsion, as promised by its prospect in high energy efficiency and potential for long driving range. However, reliable deployment of LIB in powertrains remains very challenging, and more understanding on battery performance and aging mechanisms including cell degradation under conditions specific to PHEV applications to achieve greater efficiency is desired. For a battery to reach that goal, both high energy and high power features are required.

Extensive testing of targeted cell chemistries for PHEV applications is necessary to understand each new generation of battery chemistries and their performance. Several generations of LIBs have been tested in the DOE national laboratories [1–3] using specifically designed protocols [4–7]. In this work, the targeted cell chemistry uses a positive electrode (PE) active material (PEAM) comprising $\{LiMn_{1/3}Ni_{1/3}Co_{1/3}O_2 + LiMn_2O_4\}$ composite and a negative electrode (NE) made of graphite. The concept of composite electrodes is attracting attention in recent years because it promises the combination of merits of several active materials into a hybrid electrode to allow performance optimization [8,9]. For instance, $LiMn_2O_4$ (spinel) is a promising PEAM with a high electrode potential against the Li metal reference, excellent rate capability, and relatively low cost for production; however, it exhibits a relatively low capacity, *ca.* 140–150 mAh g^{-1}, and suffers degradation from manganese (Mn^{2+}) dissolution in the electrolyte and the subsequent deposition on the NE in the charge regime to catalyze electrolyte decomposition, especially at high temperatures [9–11]. $LiMn_{1/3}Ni_{1/3}Co_{1/3}O_2$ is another promising PEAM with a higher capacity, around 180 mAh g^{-1}, but worse rate capability than the spinel. The composite composition is an ultimate compromise, which could provide an electrode that exhibits optimized capacity, rate and power capability, in contrast to more conventional PEAMs, such as alumina-coated $LiCoO_2$ (*ca.* 170 mAh g^{-1} [12]), $LiNiO_2$ (*ca.* 170–180 mAh g^{-1} [13,14]), $LiNi_xCo_{1-x}O_2$ (*ca.* 150–160 mAh g^{-1} [15]), and $LiNi_{0.8}Co_{0.15}Al_{0.05}O_2$ (*ca.* 170 mAh g^{-1} [16]). As an additional benefit, it has been found that the addition

* Corresponding author. Tel.: +1 808 956 2339; fax: +1 808 956 2336.
E-mail address: bliaw@hawaii.edu (B.Y. Liaw).

0378-7753/$ – see front matter © 2011 Elsevier B.V. All rights reserved.
doi:10.1016/j.jpowsour.2011.08.077

of the doped cobalt oxides prevents the dissolution of manganese; therefore, improving the capacity retention of $LiMn_2O_4$ upon cycling [9–11,17–21].

Through extensive testing effort, HNEI developed several useful electrochemical techniques in recent years allowing the characterization of cell-to-cell variations within a batch [22,23] as well as the understanding of how to employ such in situ electrochemical techniques [24–28] to improve the ability of extracting detailed information from data obtained from commonly used test protocols in battery performance evaluations and degradation studies.

In the initial conditioning and characterization tests (ICCT), a modified version of test protocols and procedures was derived from those defined in the *USABC Electric Vehicle Battery Test Procedures Manual* [29]. The intent of the ICCT is to establish the baseline performance matrix for the cell chemistry, including cell-to-cell variations. The cell-to-cell variations are critical to us in several aspects [22,23], including:

(1) To quantify the cell quality in performance.
(2) To quantify such variability in performance in multi-cell applications.
(3) To establish the confidence level for interpreting test results from a large matrix of cells that will undergo various test conditions.
(4) To estimate possible errors in model accuracy.
(5) To estimate possible escalation of errors in subsequent aging tests.

Another objective of the ICCT is to establish the capability for cell diagnosis with regard to degradation; particularly, the relationship of rest cell voltage (RCV) vs. state of charge (SOC) [24] and the basic features to allow incremental capacity analysis (ICA).

Subsequently various duty cycle and thermal aging tests were conducted in Idaho National Laboratory (INL) and University of Hawaii (UH), respectively. The second part of this report is to describe how to develop an in-depth understanding of the cell aging process to enable identification of cell degradation mechanism(s), so we can eventually quantify the contribution from each mechanism in the aging process. This understanding will enable the establishment of a quantitative physical model describing the degradation process for the targeted chemistry with an ability to accommodate any variance in cell degradation due to path dependence [30].

2. Experimental

Ten 1.9 Ah 18650 commercial lithium-ion cells were used in the study. The cells were surveyed by weight and open circuit voltage (OCV) measurements as received and then subjected to the ICCT using a Maccor 4300® system. All cells were tested with laboratory-made racks, and our experiences indicate that it is important to pay attention to the cable and its contact with the cell to minimize variability in the configuration of the test harnessing in order to achieve better consistency in test results and improve fidelity.

Upon the initial survey, the cells were subjected to a conditioning process using a series of charge and C/2 discharge regimes, which was terminated when the capacity was stabilized within ±0.2% between two consecutive cycles. The cells can be conditioned within 3–6 cycles typically. Unless specified, all cells were recharged using a constant current (CC) at C/2 step to 4.2 V, followed by a constant voltage (CV) step at 4.2 V until the termination current of C/25 was reached. Unless specified, the discharge cutoff voltage is generally 2.6 V. A 4-h rest between charge and discharge regimes was imposed to determine the RCV. The cells were then subjected to two discharge regimes at C/25 and C/5, after being fully recharged by the CC–CV steps each times to determine the corresponding capacity, respectively. The C/n rate represents the discharge current calculated from the nominal capacity Q_{nom} of 1.9 Ah divided by the discharge duration n in hours (h). The capacity at a specific C/n rate is denoted as Q_n. The polarization resistance of the cell is calculated from the difference in IR drops among C/25, C/5 and C/2 using Ohm's law; i.e. $\Delta V = R\Delta I$, assuming that the polarization in the cell follows a pseudo-Ohmic relationship below C/2. After these tests, the cells were recharged to 50% SOC for storage at −10 °C in a freezer.

A "nominal sample cell" or NSC was selected from the batch and subjected to additional cycling at C/25, C/5, C/2, 1C, 2C, and 5C to determine its performance characteristics. In these cycles, the cell was discharged and charged at specific rates until the cutoff condition was reached. The cell was set for 4-h rest to measure the RCV at EOC and EOD for each given rate. Remnant capacity was measured following the previous regime with a C/25 discharge or charge step to the respective cutoff condition, followed by another 4-h rest. The RCV measured at the end of this rest shall provide the SOC of the starting point for the next regime, either noted as the beginning-of-charge (BOC) or as the beginning-of-discharge (BOD), when appropriate. To determine the SOC, we used a method described in our previous work [24–28], which uses the pseudo-OCV vs. SOC (denoted as *ps*-OCV = f(SOC)) curve for this chemistry. The *ps*-OCV = f(SOC) curve is derived as follows: (1) normalize the C/25 charge and discharge ($V_{cell} = f(Q)$) curves to $V_{cell} = f(Q/Q_{25})$ curves, respectively, for the NSC. (2) Average the V_{cell} of the $V_{cell} = f(Q/Q_{25})$ curves in the charge and discharge regimes. The *ps*-OCV = f(SOC) curve has been verified to be universal within this batch. The SOC at any given condition can be determined by inferring the corresponding RCV on the *ps*-OCV = f(SOC) curve.

The incremental capacity ($-dQ/dV = f(V_{cell})$) curves are derived from correlating the amount of incremental Q (in Ah) associated with a successive voltage step, typically in 4 mV, in the charge or discharge curve to V_{cell}. The fidelity of the $-dQ/dV = f(V_{cell})$ curve is sensitive to the resolution of the data acquisition system. We typically record data in 2 mV intervals.

3. Results

3.1. Cell-to-cell variations

Fig. 1 displays (a) the weight and (b) initial OCV of the ten cells as received. According to the manufacturer's specification, the cell should weigh about 43 g. All the cells are lighter than the nominal weight with an average at 42.725 ± 0.058 g (±0.13%). The small variations on weight suggest that the manufacturing process is quite consistent. The average initial OCV recorded is 3.709 ± 0.001 V (±0.0(2)%), which corresponds to 38.2 ± 0.2% SOC according to the *ps*-OCV = f(SOC) curve [24–28]. Thus, all ten cells have almost the same SOC as received.

Fig. 2(a) shows the capacity variations obtained from C/25 and C/2 discharge regimes. The capacity measured from each of the three C/n rates (C/5 is not shown) is quite consistent among the cells, further demonstrating the consistency of the cell quality in performance. At C/2 the cells retain 1.888 ± 0.003 Ah (±0.2%) on average, whereas at C/25 a little more capacity is available with an average of 1.949 ± 0.003 Ah (±0.2%). The cells are rated at 1.9 Ah at C/2; therefore, all the cells are slightly short of the rated capacity. It is also worth noting that for rates equal to or lower than C/5 all cells are able to provide the rated capacity.

Fig. 2(b) presents the RCV at the end-of-discharge (EOD) of C/2 and C/25. As expected, the lower the rate, the lower the RCV at the EOD. At the EOD of C/25, the cell relaxed to 2.975 ± 0.005 V (±0.2%) on average, whereas at C/2 it is 3.364 ± 0.009 V (±0.3%). The consistency in the RCV at the end-of-charge (EOC) prior to the

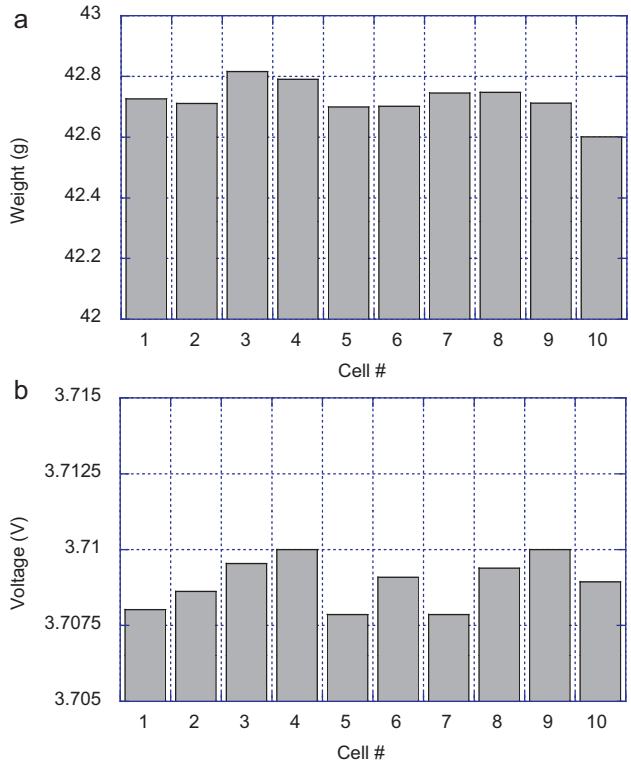

Fig. 1. (a) Weight and (b) as-received OCV for the ten commercial 18650 cells.

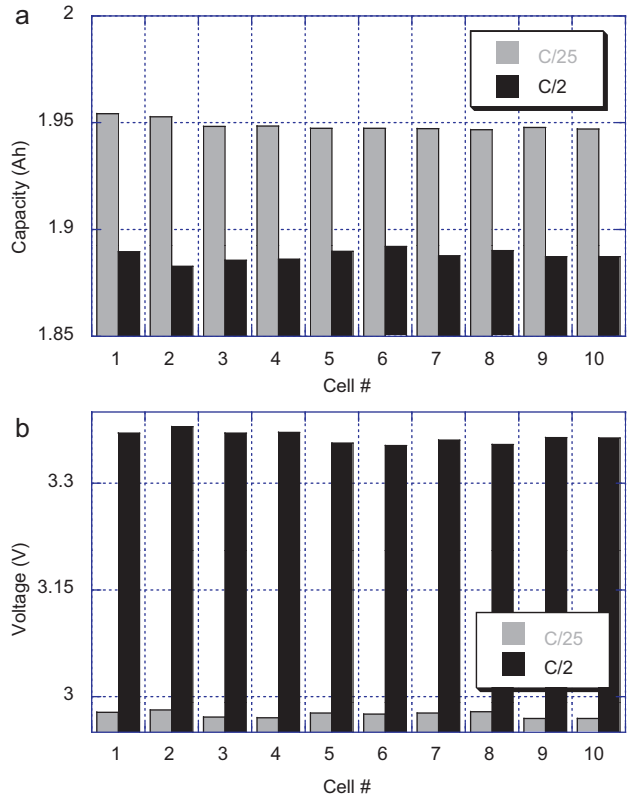

Fig. 2. (a) Capacities at C/2 and C/25 and (b) rest cell voltage (RCV) at the end-of-discharge (EOD) for the ten cells.

C/2 and C/25 discharges is even better, as the deviation is about ±0.002 V (±0.1%) on average.

Fig. 3 presents the polarization resistance derived from the discharge curves for the ten cells. The average polarization resistance

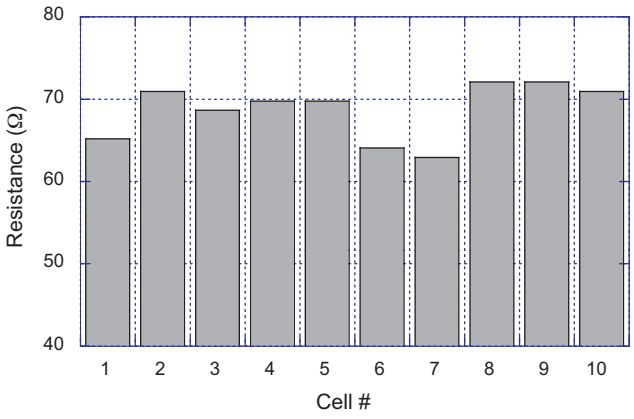

Fig. 3. Distribution of polarization resistance in the ten cells.

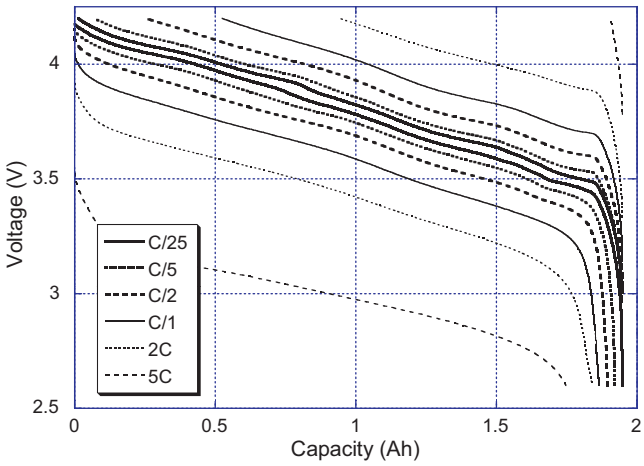

Fig. 4. Charge and discharge curves for cell #1 RPT at rates ranging from C/25 to 5C.

is 67.1 ± 3.8 mΩ (±5.7%), which contributes to little disparities in the capacity among the cells.

3.2. Initial characterization on nominal sample cell

Fig. 4 presents the $V_{cell} = f(Q)$ curves for various charge and discharge regimes in NSC during the reference performance test (RPT). It should be noted that the cell has been subjected to remnant capacity measurement at the end of each regime; therefore, the starting SOC is the same for all rates at a given regime. In Fig. 5(a), the capacity obtained from various charge and discharge regimes are reported. In the discharge regime, the capacities for rates from C/5 to 2C follow the Peukert law $Q = I^k \times t$; where k is the Peukert coefficient and t the nominal discharge time (in h). The Peukert coefficient $k = 1.019$ was determined, which indicates that the cell has reasonable rate capability. However, the Q_{25} appears to be lower than that extrapolated from the Peukert equation (1.949 Ah vs. 1.998 Ah), suggesting that the cell maximum capacity in this voltage range is reached. The capacity at 5C is below the value extrapolated from the Peukert equation. The Peukert law primarily takes into account the capacity variability originated from variations in mass transfer in the porous electrodes. It does not take into account any polarization effect. It assumes that all electrode reactions were completed at a given rate. Judging from the voltage response in the 5C discharge regime as shown in Fig. 4, it appears that the cutoff voltage has been reached prior to the completion of the electrochemical reactions at the surface of the electrodes. We further verified that the cutoff was indeed reached prematurely

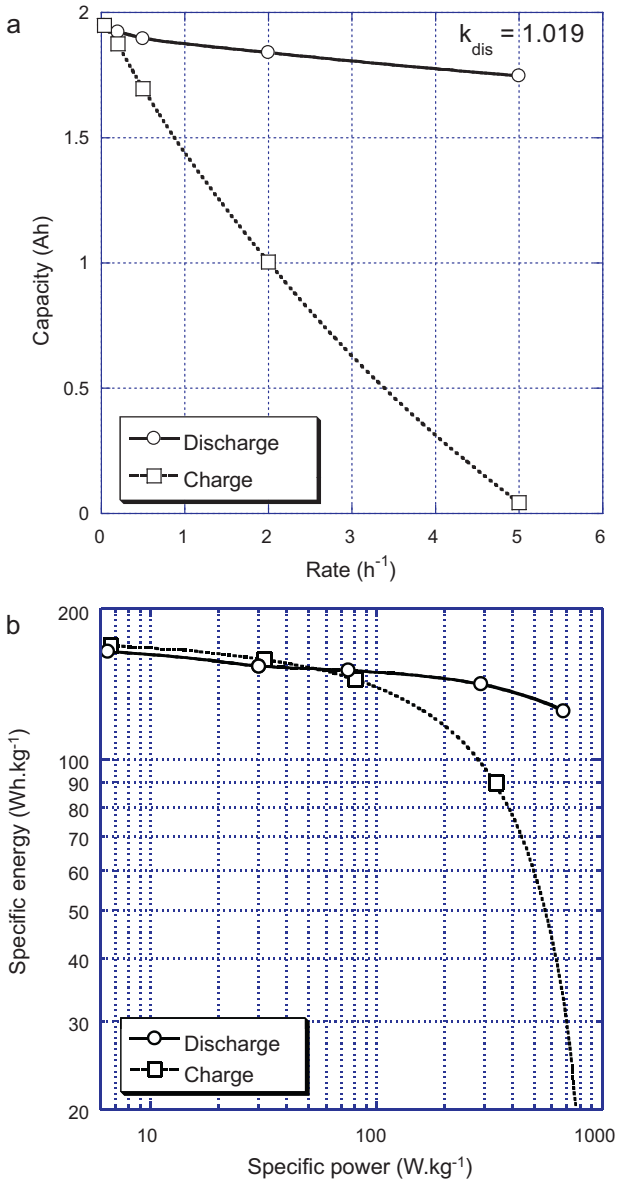

Fig. 5. (a) Peukert plot and (b) Ragone plot of cell #1 RPT.

before the knee that is typical for the EOD. This premature cutoff explains why the 5C capacity does not follow the Peukert law.

In the charge regime, due to the same constraint and premature cutoff, the rate-dependent charge return did not follow the Peukert law either. It is understandable that, due to the stability window of the electrolyte and the nominal cell voltage, which is close to 3.7 V, the cell has a 1.0 V margin in the discharge regime; yet, only 0.5 V in the charge regime, to accommodate polarization. It is therefore, similar to most of the high-voltage chemistries, that this cell chemistry is susceptible to overcharging under high-power pulse charging conditions (such as in regenerative breaking).

Conventionally, the power capability of the cell should be determined by constant power discharge tests. The assessment of power capability could be approximated by the power requirements derived from constant current tests by multiplying the average voltage with the C/*n* rate current. Such an estimate of power capability often results in an underestimate from the one by constant power test because in the case of constant current discharge the polarization increases more aggressively toward the EOD and leads to a lower power amplitude. Nevertheless, this approximation provides a reasonable estimate of the trade-off between power and energy for this chemistry, as revealed in the Ragone plot in Fig. 5(b). The cell is able to deliver 125 Wh kg^{-1} at 650 W kg^{-1}, indicating a good power capability of this chemistry. In the charge regime, however, the energy absorbable by the cell drops below 100 Wh kg^{-1} at 250 W kg^{-1}, suggesting that the chemistry cannot handle high charge rates for fast charging or regenerative braking over a considerable range of high SOC.

4. Discussion

4.1. Cell-to-cell variations

We recently demonstrated that, using common testing procedures and techniques to analyze the conditioning cycles of 100 cells provided by a vendor, three attributes were derived to characterize the cell variations: the amount of active material in the cell, polarization resistance, and other kinetic factors that confine the rate capability [22,23]. The amount of active material dictates the maximum capacity in a cell. The polarization resistance dictates the cell voltage under polarization, thus the portion of capacity and power deliverable under a certain rate and cutoff conditions. Finally, the rate capability, the capability of a cell in handling discharge rate variations, is dictated by the additional kinetic factors, as expressed by the Peukert coefficient.

The amount of active material in the cell can be determined by the capacity released at a very slow rate such as C/25 or less; or, from a process that determines the quantity called "capacity ration," in Ah %SOC^{-1}, which is derived from the capacity at a given rate and the RCVs measured at EOC and EOD that denote the SOC range involved in delivering the said capacity. From the RCVs, the SOC range can be determined from the *ps*-OCV = f(SOC) curve for the given rate. Dividing the capacity with this SOC range, the "capacity ration" is thus calculated [22,23]. It is important to

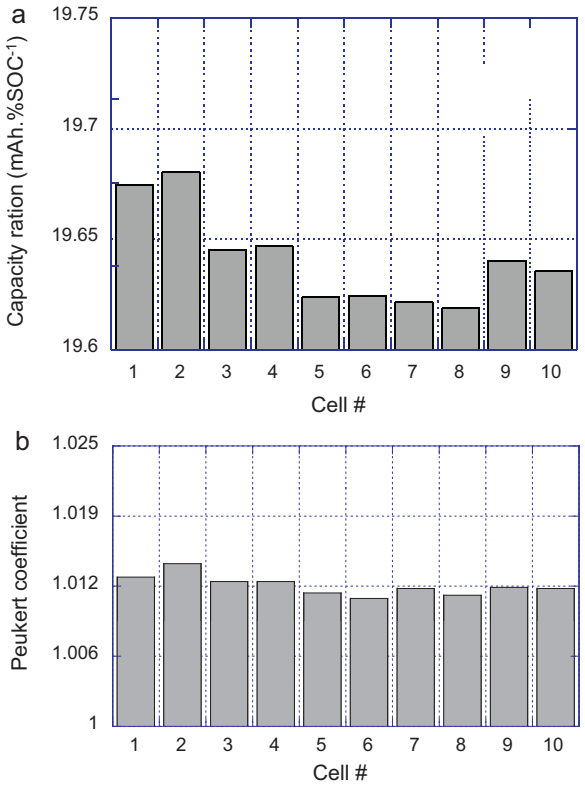

Fig. 6. (a) Capacity ration and (b) Peukert coefficient variations for the 10 cells.

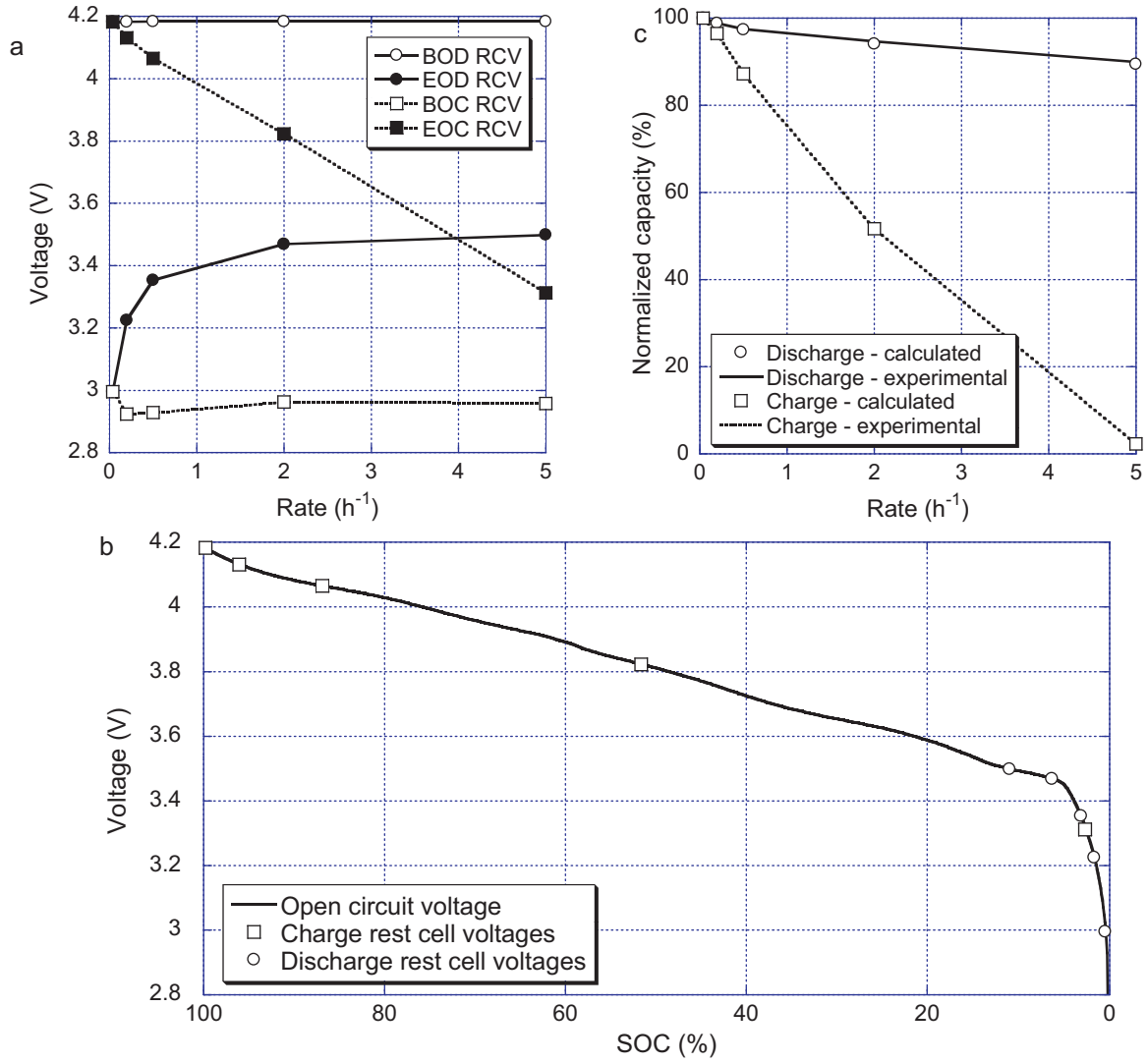

Fig. 7. (a) Evolution of the RCV with rate, (b) *ps*-OCV = f(SOC) curve calculated from C/25 charge discharge curves, and (c) the correspondence of SOC range between BOD and EOD and capacity at various rates.

recognize that the two methods depicts the same concept that the truly meaningful SOC can only be determined by electrochemical equilibrium, in which the range of SOC should coincide with the capacity at any rate; and, such a "capacity ration" associates with and defines the content of the active materials in the cell. It is also important to note that the capacity ration is thus rate independent.

The additional kinetic constraints other than the polarization resistance are usually introduced in the manufacturing processes, e.g. inhomogeneity arisen from differences in the electrode thickness, additive ratio, and/or electrode porosity [31,32]. We postulated that these factors would influence the effective utilization of active material in general and thus induce variations in the rate capability performance of a given cell, which can be represented by variations in the Peukert coefficient. The variation in the rate capability can be estimated from the capacities measured in the ICCT (thus, at C/25, C/5 and C/2).

Fig. 6 presents the values of (a) the capacity ration and (b) Peukert coefficient for the ten cells. The average capacity ration is 19.66 mAh %SOC^{-1} and its deviation among the cells is ±0.2%. The average Peukert coefficient is 1.013 ± 0.1%. The small deviation observed indicated that the intrinsic quality of the cell assembly is rather consistent, as shown by the rate capability. The polarization resistance (shown in Fig. 4) varies between 63 and 72 mΩ (about 6% in deviation).

The overall performance variations among the cells are relatively insignificant, compared to other results of different cell chemistries we measured so far. The discharge curves among the cells can be superimposed upon one another even at C/2, which indicates that the cell technology may support intended PHEV well in pack applications and that the results of the NSC can be extended to others in the batch.

4.2. Initial characterization on nominal sample cell

Fig. 7(a) presents the evolution of RCV for each charge and discharge regime as a function of C rate. Since the same remnant capacity measurement and a 4-h rest were imposed at the end of each regime, RCVs at BOC or BOD are rather independent of C rate; thus, all regimes start with almost the same SOC at BOC or BOD, respectively. However, the RCVs at EOC or EOD vary. The EOC RCVs follow a linear relationship with C rate, suggesting that the cut-off was primarily determined by polarization. The EOD RCVs are a strong function of C rates below 1C and approach a steady value after 2 C. To understand this behavior, we refer the RCVs to the *ps*-OCV = f(SOC) curve as shown in Fig. 7(b). A voltage plateau exists

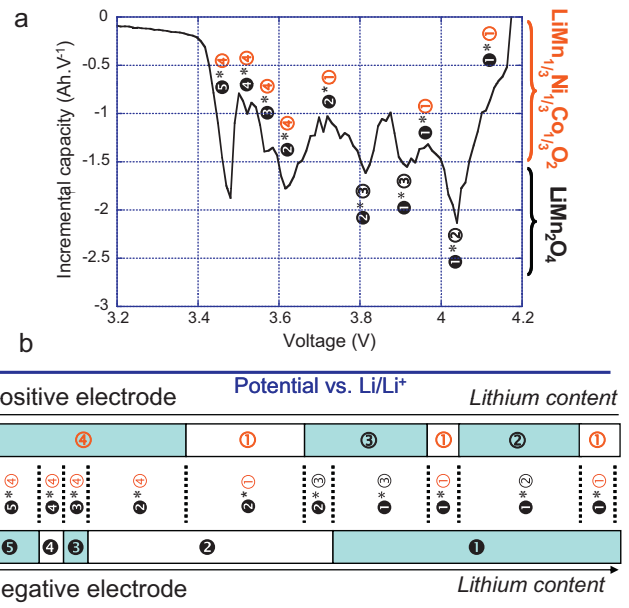

Fig. 8. (a) Incremental capacity (IC) signature of cell #1 at C/25 and (b) schematic presentation of the cell reactions in the IC peak index.

around 3.5 V, which explains why the RCVs remain rather constant for 2C and 5C, whereas the capacity varies substantially. The presence of the plateau on the *ps*-OCV = f(SOC) curve indicates that both electrodes undergo phase transformations. These reactions are discussed in details in Fig. 8 and this plateau is shown to be associated with a graphite staging.

Fig. 7(c) presents the comparison between the capacities normalized with Q_{25} in the test and calculated from the RCVs (the corresponding SOCs inferred from Fig. 7(b)). The excellent agreement supports the validity of our approach in using *ps*-OCV = f(SOC) curve inference to determine SOC. Several implications arise from such validity. The mixed oxide cathode and carbonaceous anode in the cell chemistry should follow the core–shell model and Li diffusion from the surface to the core of the grains is the rate-limiting step in the cell reaction and relaxation process. The rate of diffusion is probably comparable to C/8, as suggested by the achievement of the maximum capacity at this rate (as estimated from the Peukert equation). Therefore, at rates lower than C/8 all the active materials are involved in the electrochemical reactions to achieve the maximum capacity, whereas at rates higher than C/8 the core of the grains remains deficit in Li up-taking; thus, only partial capacity is delivered.

The targeted cell chemistry in this work employs a composite PE (c-PE) comprising $\{LiMn_{1/3}Ni_{1/3}Co_{1/3}O_2 + LiMn_2O_4\}$ and a graphite NE. Thus, a complex cell incremental capacity (IC) signature is expected. Although a more definitive derivation of the IC signature should be performed from half-cell experiments for both electrodes in reference to Li metal, it is unfortunately impossible for us to conduct such experiments. Therefore, to infer such complex electrode reactions in reference to the IC signature can only be synthesized from literature reports. If the two active materials in the c-PE do not interfere with each other, we infer that IC signals of each active material in the c-PE shall be convoluted with those of the graphite NE, resulting in a series of distinct IC peaks. Fig. 8(a) shows the IC behavior of the NSC discharged at C/25 and Fig. 8(b) displays the peak index based on electrode reactions inferred from those reported in the literature [32–36].

In the PE potential range vs. a lithium reference electrode in this study, $LiMn_{1/3}Ni_{1/3}Co_{1/3}O_2$ presents a steady potential decrease from 4.2 V to 3.75 V in the solid solution region in the hexagonal phase. Further Li intercalation in the crystal structure leads to a phase transformation to the rock salt phase and exhibits a potential plateau at 3.75 V [35,36]. In the case of $LiMn_2O_4$ two potential plateaus at 4.1 V and 3.95 V are reported for two phase transformations [34]. Accordingly, two IC peaks, a sharper one at 4.1 V and another with a broader asymmetric shape at 3.95 V; are thus expected. Summarized from these literature reports, we can then infer the IC curve for the c-PE with four IC peaks as follows: the first peak (a broad band from 4.2 V to 3.75 V) is the one for the solid solution region in $LiMn_{1/3}Ni_{1/3}Co_{1/3}O_2$ (①). Within this broad potential range, the two peaks (4.1 V and 3.95 V) in $LiMn_2O_4$ (② and ③) shall intrude before the phase transformation in $LiMn_{1/3}Ni_{1/3}Co_{1/3}O_2$ (④) takes place at 3.75 V.

In the NE, when discharged, the lithiated graphite undergoes five distinct phase transformations, as denoted by ❶ to ❺, according to the literature [32]. Fig. 8(b) summarizes the reactions in the two electrodes on a unified potential scale. In order to index the IC peaks by their distinctive reactions in the electrodes, we use the following notation as convention: (1) an IC peak is a unique representation of a NE reaction convoluting with a corresponding one on the positive, (2) the NE reaction is denoted by a black (filled) numbering, while the positive with an open (unfilled) one, (3) using "*" to denote the convolution between the negative and positive IC signals that results in the unique IC peak in the cell. Thus, the peak indexed as ❶ *② represents reaction ❶ in the NE convoluting with reaction ② in the PE.

From the indexing, we found that some features of the IC peaks can be used as status indicators for an electrode (or its constituents), if a potential plateau is present on the opposite electrode. For instance, peak ❶ *② may reveal the status of the state of $LiMn_2O_4$, since ❶ is on a potential plateau; likewise, peak ❷ *④ is an indicator for $LiMn_{1/3}Ni_{1/3}Co_{1/3}O_2$, and peak ❺ *④ for the graphite electrode. In addition, the position and area of a few specific IC peaks can be used to estimate the composition ratio between the two PE constituents. By examining the IC peak area associated with ④ , which accounts for 1/3 the total cell capacity, as well as half the $LiMn_{1/3}Ni_{1/3}Co_{1/3}O_2$ capacity, we thus conjecture that the c-PE composition likely comprise 2/3 of $LiMn_{1/3}Ni_{1/3}Co_{1/3}O_2$ and 1/3 of $LiMn_2O_4$. Similarly, by examining the capacity associated with peaks ❶ on the NE we can estimate the loading ratio between PE and NE (after the initial SEI formation on the NE). Ideally, ❶ accounts for half of the capacity of a typical graphite NE, since it corresponds to the transformation from LiC_{12} to LiC_6. A useful approach to determine the electrode-loading ratio is to study the capacity measured at low rates, in which the liberation of capacity undergoes with a minimal influence from kinetics while delivering its maximum Ah content in the active materials in the cell. For instance, the *Q* associated with ❶ is 41.5% of the cell capacity. Since the graphite is near complete Li depletion at the EOD (as conjectured by the presence of peak ❺ and its tail), 41.5% of the NE capacity must have been employed in the discharge regime. On the other hand, due to the irreversible loss of Li inventory typically occurs in the first cycle of the formation, most of the cell design is loaded with NE in excess of capacity in order to capture the full capacity of the PE. As such, the PE loading usually is the one limiting the cell capacity. Therefore, after the initial SEI formation, only 91.5% of the capacity (41.5% from ❶ and nearly 50% from the remaining) in the graphite is utilized. We thus conjecture that the loading ratio of NE/PE is around 1.08.

Fig. 9(a) and (b) presents the IC curves associated with different cycling rates. At the first glance, they all appear similarly in behavior, except for 5C, which exhibits a significant change in behavior during discharge and almost no signature during charge, likely due to a high degree of polarization. In order to compare IC curves of different rates, it is easier to exhibit them in terms of IR-free voltage instead of the measured cell voltage. The polarization resistance in the charge and discharge regimes is thus needed. Fig. 10 presents

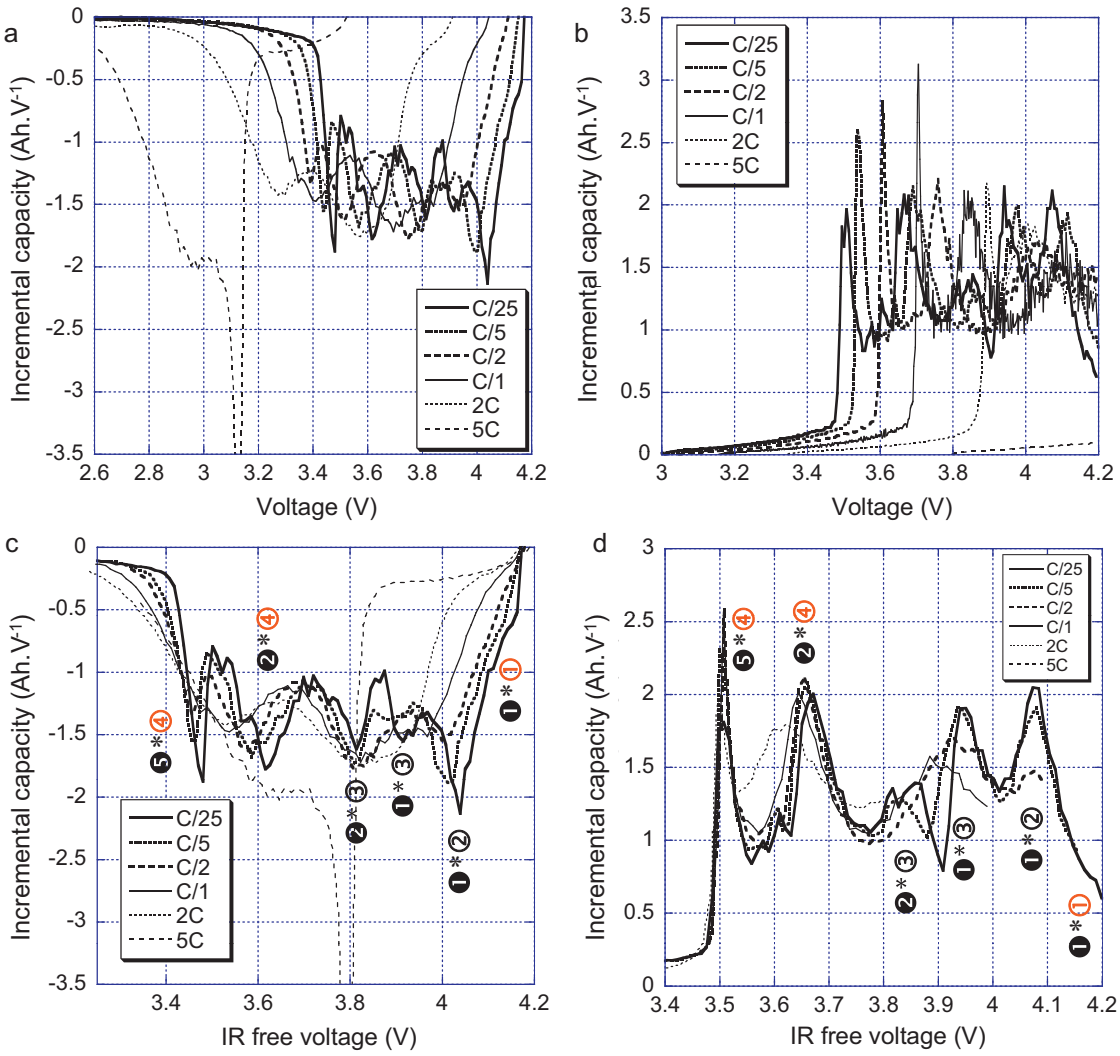

Fig. 9. Rate effect reflected in the IC curves in (a) discharge and (b) charge with polarization, while (c) and (d) present the same without polarization.

the evolution of the cell voltage as a function of the IR drop at (a) the BOD and (b) the beginning-of-charge (BOC) at different rates. Since all rates have almost the same starting SOC, the initial IR drop can be used to determine the cell internal resistance at both BOD and BOC. Only rates lower than 1C were used to ensure that the observation is still in the ohmic regime of the Tafel behavior, where the voltage response to current is linear. The polarization resistance was found to be 132 mΩ Ah and 216 mΩ Ah, or 69 mΩ and 114 mΩ, respectively, at BOD and BOC for the NSC. It indicates that the resistance at the BOC is significantly higher than that at the BOD.

Fig. 9(c) and (d) presents the IC curves without polarization-induced voltage drop for a better comparison of the IC peaks in the discussion. The rate effect on the cell behavior can be separated into two parts: one for the rates below 1 C and the other above. For the lower rates only peak broadening is observed, indicating that the solid-state diffusion remains as the rate-limiting factor. The peaks in the low voltage region of the discharge regime and the high voltage region of the charge regime appear more broadened than those in the other regions, likely a result of the grain size (long diffusion path).

Substantially different behavior in the IC peaks was observed for the higher rates. It seems that all IC peaks with ❶ are fading in rate capability as the rate increases. This phenomenon is not peculiar, as it is known that reaction ❶, which corresponds to the transformation of LiC_6 to LiC_{12}, is kinetically slower than other anodic reactions leading to the lithium depletion in the graphite structure. Therefore, the peaks associated with ❶ (thus, ❶ *(① , ② , and ③ , respectively)) are broadened more than the others as the rate increases and start to overlap with peaks associated with reaction ❷, especially ❷ *③. This behavior leads to a longer time-resolved extent of reaction, as on the surface of the active grains, the cell voltage indicates that reactions ❷ *(②, ③ respectively) have already occurred, whereas in the core the composition remains at ❶ *(② and ③ , respectively) and needs to catch up with the surface reaction. An extreme case is observed in 5C, where reaction ❶ *① occurs slowly throughout the grain, while the cell voltage as measured on the grain surface is approaching reaction ❷. This phenomena and their consequence, as exhibiting on IC signals, continue to play out in the cell reactions in a dynamic manner, explaining the extremely broadened peak in convolution at this rate.

As a general trend, it appears that $LiMn_{1/3}Ni_{1/3}Co_{1/3}O_2$ is affected by the increase of current (rate) more than $LiMn_2O_4$ (thus, worse rate capability). The evolution of peaks ❶ *① and ❶ *② explains. The transition from ① to ② occurs on the staging plateau ❶ , which eliminates the contribution from the NE to the change of the peak shape over cycling. Upon cycling, peak ❶ *① is clearly broadened, delaying the onset of the next reaction; whereas, the shape of peak ❶ *② appears only slightly affected. This observation affirms that $LiMn_2O_4$ is a constituent that has higher rate capability for

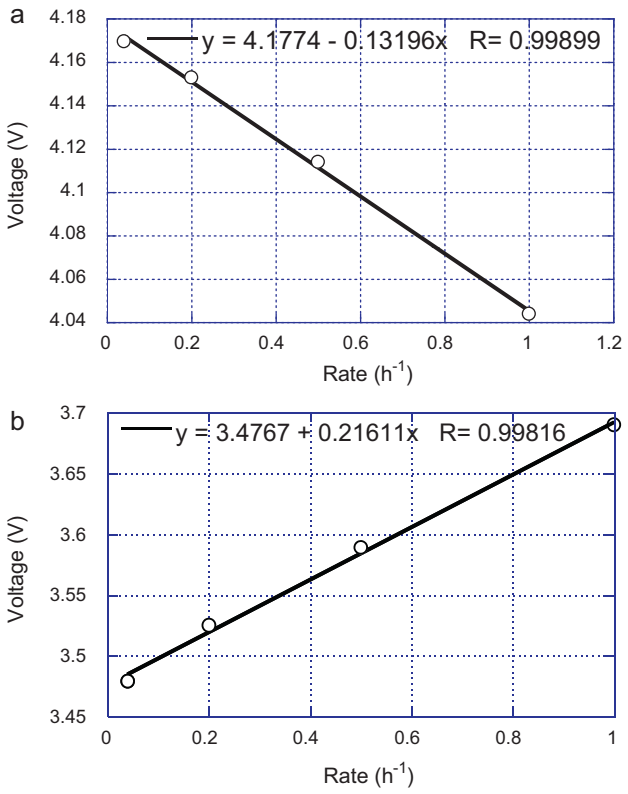

Fig. 10. Evolution of the cell voltage due to IR drop as a function of rate at (a) BOD and (b) BOC in cell #1.

high power delivery, whereas the $LiMn_{1/3}Ni_{1/3}Co_{1/3}O_2$ contributes more to the capacity.

Change in behavior of the IC peaks over aging shall give us a vantage point to infer mechanisms that affect capacity. Seeing how active materials and their constituents change over time and aging conditions will be informative toward improving cell design and choice of materials, as well as exploiting the best conditions for which to use these materials. This information will be incorporated into physics-based degradation models to elucidate further knowledge for root-causes of cell aging and will be discussed in the part II of this work.

5. Conclusion

A batch of ten 1.9 Ah commercial 18650 cells was investigated to characterize its baseline performance and intrinsic cell-to-cell variations. It was found that the cells are of high quality with little cell-to-cell variations, thus establishing a high confidence level for analyzing and interpreting test results from a large matrix of cells that undergo various test conditions. Moreover, these cell variations should be incorporated and accommodated into future cell and pack performance models and simulations to enhance accuracy in prediction.

The analysis of the incremental capacity (IC) curves showed that the complex IC signature could be deciphered and that information on each specific active component in the cell, $LiMn_{1/3}Ni_{1/3}Co_{1/3}O_2$ and $LiMn_2O_4$, in the PE and graphite in the NE, could be gathered respectively. From the analysis of the relative IC peak capacity in some of the reactions specific in each components, we are able to conjecture that the c-PE comprises about 2/3 of $LiMn_{1/3}Ni_{1/3}Co_{1/3}O_2$ and 1/3 $LiMn_2O_4$, and similarly that, after the initial SEI formation, the loading ratio of NE/PE is about 1.08. This inference ability to deciphering IC behavior in the cell chemistry has profound potential to analyzing the degradation of the cell in the second part of this study. This implication is important to us, as these cells are intended to support the design of an experiment that uses a large matrix of cells and test conditions to study path dependence of cells' degradation under PHEV duty cycles and conditions. Between UH and INL more than 60 cells are under testing with different aging protocols. The result of this study on cell variations established a reliable basis for comparison of future aging test results. It also helps to establish a consistent diagnostic methodology to enable a higher possibility of success in this experiment and to assure that the observed discrepancies in the test data can be attributed to aging protocols with certain confidence.

Acknowledgements

The authors gratefully acknowledge funding provided by the Office of Energy Efficiency and Renewable Energy of the United States Department of Energy (Contract No. DE-AC07-05ID14517).

References

[1] R.B. Wright, C.G. Motloch, J.R. Belt, J.P. Christophersen, C.D. Ho, R.A. Richardson, I. Bloom, S.A. Jones, V.S. Battaglia, G.L. Henriksen, T. Unkelhaeuser, D. Ingersoll, H.L. Case, S.A. Rogers, R.A. Sutula, J. Power Sources 110 (2002) 445.
[2] Idaho National Laboratory, Gen 2 GDR Performance Evaluation Report, INL/EXT-06-11488, revision 4, July 2006.
[3] I. Bloom, L.K. Walker, J.K. Basco, D.P. Abraham, J.P. Christophersen, C.D. Ho, J. Power Sources 195 (2010) 877.
[4] Advanced Technology Development Program For Lithium-Ion Batteries: Battery Technology Life Verification Test Manual, INEEL/EXT-04-01986, February 2005.
[5] FreedomCAR Test Plan for Advanced Technology Development Gen 2 GDR Cells, EHV-TP-152, Revision 3, July 2004.
[6] FreedomCAR Battery Test Manual for Power-Assist Hybrid Electric Vehicles, DOE/ID-11069, October 2003.
[7] Idaho National Laboratory, Battery Test Manual for Plug-in Hybrid Electric Vehicles, INL/EXT-07-12536, revision 0, March 2008.
[8] J.W. Fergus, J. Power Sources 195 (2010) 939.
[9] P. Albertus, J. Christensen, J. Newman, J. Electrochem. Soc. 156 (2009) A606.
[10] B. Scrosati, J. Garche, J. Power Sources 195 (2010) 2419.
[11] Z.F. Ma, X.Q. Yang, X.Z. Liao, X. Sun, J. McBreen, Electrochem. Commun. 3 (2001) 425.
[12] J. Cho, Y.J. Kim, B. Park, J. Electrochem. Soc. 148 (2001) A1110.
[13] W. Li, J.N. Reimers, J.R. Dahn, Solid State Ionics 67 (1993) 123.
[14] J. Barker, R. Koksbang, M.Y. Saidi, Solid State Ionics 89 (1996) 25.
[15] C. Delmas, I. Saadoune, Solid State Ionics 53–56 (1992) 370.
[16] M. Broussely, Ph. Blanchard, Ph. Biensan, J.P. Planchat, K. Nechev, R.J. Staniewicz, J. Power Sources 119–121 (2003) 859.
[17] T. Numata, C. Amemiya, T. Kumeuchi, M. Shirakata, M. Yonezawa, J. Power Sources 97 (2001) 358.
[18] H. Kitao, T. Fujihara, K. Takeda, N. Nakanishi, T. Nohma, Electrochem. Solid-State Lett. 8 (2005) A90.
[19] S.-T. Myung, M.H. Cho, H.T. Hong, T.H. Kang, C.-S. Kim, J. Power Sources 146 (2005) 222.
[20] A. Manthiram, W. Choi, Electrochem. Solid-State Lett. 10 (2007) A228.
[21] N.V. Kosova, E.T. Devyatkina, V.V. Kaichev, A.B. Slobodyuk, Solid State Ionics 192 (2011) 284.
[22] M. Dubarry, N. Vuillaume, B.Y. Liaw, J. Power Sources 186 (2009) 500.
[23] M. Dubarry, N. Vuillaume, B.Y. Liaw, Int. J. Energy Res. 34 (2010) 216.
[24] M. Dubarry, V. Svoboda, R. Hwu, B.Y. Liaw, J. Power Sources 165 (2007) 566.
[25] M. Dubarry, V. Svoboda, R. Hwu, B.Y. Liaw, J. Power Sources 174 (2007) 1121.
[26] M. Dubarry, B.Y. Liaw, J. Power Sources 194 (2009) 541.
[27] M. Dubarry, B.Y. Liaw, J. Power Sources 196 (2011) 3420.
[28] M. Dubarry, B.Y. Liaw, J. Electrochem. Soc., to be submitted for publication.
[29] Gary Hunt et al., USABC Electric Vehicle Battery Test Procedures Manual, Revision 2, January 1996.
[30] K.L. Gering, S.V. Sazhin, D. Jamison, C.J. Michelbacher, B.Y. Liaw, M. Dubarry, M. Cugnet, J. Power Sources 196 (2011) 3395.
[31] C. Fongy, A.C. Gaillot, S. Jouanneau, D. Guyomard, B. Lestriez, J. Electrochem. Soc. 157 (2010) A885.
[32] C. Fongy, S. Jouanneau, D. Guyomard, J.C. Badot, B. Lestriez, J. Electrochem. Soc. 157 (2010) A1347.
[33] D. Aurbach, B. Markovsky, I. Weissman, E. Levi, Y. Ein-Eli, Electrochim. Acta 45 (1999) 67.
[34] T. Ohzuku, M. Kitagawa, T. Hirai, J. Electrochem. Soc. 137 (1990) 769.
[35] K.W. Nam, W.S. Yoon, H. Shin, K. Chung, J. Power Sources 192 (2009) 652.
[36] N. Yabuuchi, T. Ohzuku, J. Power Sources 119–121 (2003) 171.